Stepwise Fabrication and Optimization of Coplanar Waveguide Resonator Hybrid Devices

Nicole Kellner, Niklas Hüttner, Marco Will, Pertti Hakonen, and Andreas K. Hüttel*

From the background of microwave-optomechanical experiments involving carbon nanotubes, the optimization of superconducting coplanar waveguide resonator devices is discussed. Two devices, one with unmodified geometry compared to previous work and one integrating several improvements, are lithographically built up step-by-step. After each step, the low-temperature GHz transmission properties are retested. This allows to identify the impact of the fabrication and the geometry modification on the device properties. In addition, simplified circuit geometries are modeled numerically, confirming the experimental results and providing further insights for optimization.

1. Introduction

Research in the field of optomechanics[1] has over the past years covered a wide range of material systems and parameter ranges. In terms of frequencies, experiments reach from optics to microwave technology; mechanical systems can be single atoms or macroscopic mirrors. In a comparatively recent development, also carbon nanotubes have been integrated with dispersive microwave optomechanical circuits.[2,3] Given their high mechanical quality factors at cryogenic temperatures[4,5] and their properties as prototypical single electron devices,[6] this paves the way for novel combinations of quantum transport and optomechanical manipulation.

The central limitation of the device measured in previous studies,[2,3] with the geometry as also shown in **Figure 1**a–c, was a very low quality factor $Q_c \approx 500$ of the microwave resonator. While also fabrication defects may have played a role there, with

N. Kellner, N. Hüttner, A. K. Hüttel
Institute for Experimental and Applied Physics
University of Regensburg
Universitätsstr. 31, 93053 Regensburg, Germany
E-mail: andreas.huettel@physik.uni-regensburg.de

M. Will, P. Hakonen, A. K. Hüttel
QTF Centre of Excellence
Department of Applied Physics
Aalto University School of Science
P.O. Box 15100, 00076 Aalto, Finland

The ORCID identification number(s) for the author(s) of this article can be found under https://doi.org/10.1002/pssb.202300187.

fluorinated resist flakes stuck to the central conductor of the coplanar waveguide,[2,3] the main challenge is a more systematical one. Previous work in Regensburg has demonstrated standalone high-Q_c resonators.[7] Inserting and contacting carbon nanotubes into the device[8] and performing both quantum transport and microwave transmission measurements, however, require the definition of dc electrodes close to the coplanar waveguide resonator or even attaching to it. These immediately lead to leakage of the GHz field.

Here, we present data on the fabrication and characterization of two niobium devices, A and B. Device A is geometrically close to the device of previous studies,[2,3] while device B integrates larger filters to block the signal leakage as well as further improvements. After each lithographic step, the devices are cooled down and the resonator properties are tested at $T = 4.2$ K. This allows us to identify the fabrication steps detrimental to Q_c as well as validate the effect of our optimizations. Subsequently, the transmission of simplified device geometries is modeled numerically, clearly confirming our experimental result and providing insight into the detailed mechanisms.

2. Device Geometry and Fabrication, Device A

Figure 1 displays the geometry of the two analyzed devices. In each case, the substrate is a wafer of 500 μm compensation-doped silicon covered by 500 nm thermally grown SiO_2 and a 100 nm niobium film. Figure 1a shows the full lithography drawing of device A, in its geometry identical to the device used in previous studies;[2,3] Figure 1b,c shows details of it.

As the first fabrication step (step 1 in **Table 1**), the coplanar waveguide resonator, the dc bond pads, and their connecting lines are patterned in the niobium film using optical lithography (blue layer in Figure 1a–c). Positive resist Microposit S1813 is spin-coated, exposed with a mask-aligner, and developed using developer AZ300-47. For the etch process, argon and sulfur hexafluoride are used in an Oxford Plasmalab reactive ion etching (RIE) system.

Next, electron beam lithography is used to define the 100 nm wide gate finger (red, in the center of Figure 1c; step 2 in Table 1). A polymethyl methacrylate (PMMA) bilayer (first layer molecular weight 200 k 9% in anisole, second layer 950 k 2% in anisole) is spin-coated, exposed, and developed with a mixture of methyl isobutyl ketone (MIBK) and isopropanol (IPA) in volume ratio 1:3. 10 nm titanium as adhesive layer is sputter-deposited,
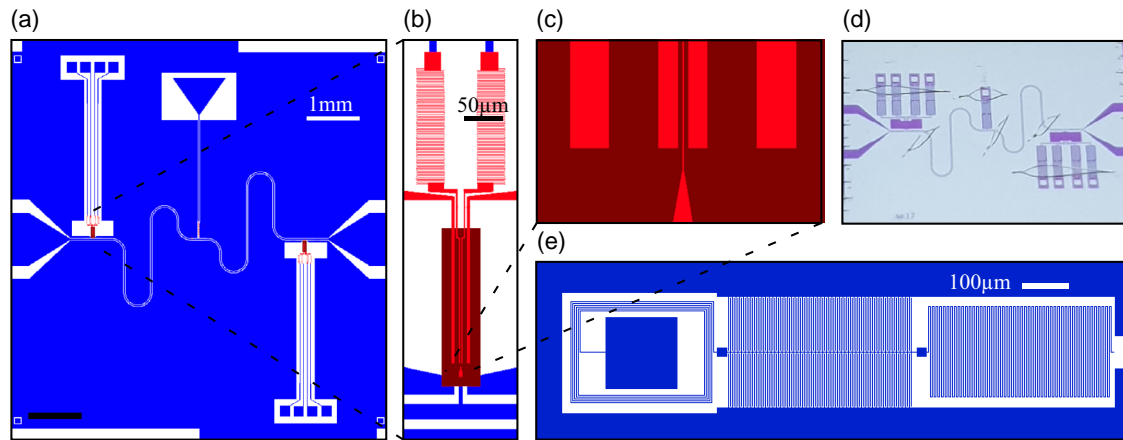
Figure 1. a) Overall geometry of device A. Blue: niobium layer, white: etched region with bare substrate surface, brown: gate insulator, red: gold electrodes and meanders. b) Detail zoom of (a) in the carbon nanotube transfer region.[8] c) Detail zoom of (b), showing the gate finger between the source/drain contacts. Note that in the actual device the gate finger lies below, the contacts, however, above the gate insulator. d) Overview photograph of device B after bonding. e) Filter circuit as added to each of the dc connections in device B, consisting of a coil inductor, an interdigital capacitor, and a meander inductor.

Table 1. Coplanar waveguide resonator quality factors Q_c of devices A and B measured after subsequent lithographic fabrication steps. Some of the mentioned elements are only present in one device; see the text for details. In particular, A contains only Au-based filters, while B contains only Nb-based filters.

Measured Q_c at $T = 4.2\,K$		Device	
after fabrication step		A	B
1	Resonator, dc connections, Nb filters, bond pads	2500	2400
2	Gate finger electrode in the transfer area	1800	1200
3	Cross-linked PMMA gate insulator	1600	
4	Central Au filter, connection resonator-filter	1600	
5	Contact electrodes in the transfer area, Au filters	420	1600
6	Deep etching of the adjacent trenches	460	1700

followed by thermal evaporation of 50 nm gold and lift-off in hot acetone.

In the following step, the gate insulator (brown in Figure 1a–c; step 3 in Table 1) is deposited as cross-linked PMMA: a PMMA bilayer is spin-coated and locally overexposed by a factor ≈ 20. This leads to cross-linking of the resist molecules and thus a ≈ 200 nm thick insulator layer insoluble in acetone and other process solvents, with a low relative dielectric constant of typically $\varepsilon_{PMMA} \simeq 3$.[9]

Subsequently, the meander filter for the gate contact at the center of the resonator (red in Figure 1a, step 4 in Table 1) is defined, again via electron beam lithography with a PMMA bilayer, metallization, and lift-off; here the gold thickness is 200 nm. The gold meander has a strip width of 500 nm and consists of 160 turns of each 18 μm length.

This is repeated for the four contact electrodes (source, drain, and two cutting electrodes) in the transfer area and the meander filters connecting them (again, red in Figure 1a–c, step 5 in Table 1). The gold meanders for the four contacts have ≈ 120 turns of each 35 μm length.

As the last step, deep trenches are etched on both sides of the contact electrodes to allow insertion of the quartz forks during nanotube transfer (geometry not shown in the figure; step 6 in Table 1).[8] We spin-coat two layers of AZ9260 photoresist and expose it using a mask aligner. AZ400K:water in ratio 1:2 is used as developer, followed by RIE etching with argon and sulfur hexafluoride to a depth of ≈ 10 μm.

3. Device Geometry and Fabrication, Device B

Device B, as shown in Figure 1d,e, is an improved version where both the device geometry and (out of necessity) the fabrication steps have been adapted. The most distinct change is the introduction of niobium-based T-filters in each dc connection,[10] as shown in Figure 1e. These consist of a spiral inductor around a bond pad with 2 μm thick turns separated by a 2 μm wide gap, an interdigital capacitor that couples to the ground plane via 100 meshing fingers on both sides, 117 μm long and 2 μm wide separated by gaps of 2 μm, and finally a meander inductor 2 μm wide, separated by 2 μm gaps, with 100 turns of each 198 μm length. For the definition of the coplanar waveguide resonator, a generic photomask without dc contacts is used; the filters are added subsequently via electron beam lithography and a second identical reactive ion etching process patterning the niobium layer (i.e., included in step 1 in Table 1).

To reduce the capacitive coupling between the gate finger and contact electrodes, the contact electrodes (step 5) are additionally shortened; the "coupling length" L, where gate and contacts run in parallel, is reduced from about 155 μm in device A to 86 μm in device B.

4. Transmission Measurements at 4.2 K

To identify detrimental processes, the devices were glued onto a sample carrier, bonded, and cooled down in a liquid helium

vessel for microwave transmission measurement after each fabrication step. The temperature of the liquid helium, $T = 4.2\,\text{K}$, is close enough to the critical temperature of niobium $T_{\text{Nb}} = 9.2\,\text{K}$ to still lead to a reduction of intrinsic resonator quality factors,[7,11–13] however, any fabrication-induced reduction that is already visible here will also impact measurements at a lower temperature. Thermalization of the device was done directly by immersion into the liquid helium, without any further low-temperature attenuation or isolation of the cables.

Figure 2 displays example transmission measurements. The curve of Figure 2a shows the transmission of device B directly after definition of the coplanar waveguide resonator (step 1), at a vector network analyzer (VNA) output power $P = -20\,\text{dBm}$. Figure 2b shows a large frequency range plot of the difference in dB of two transmission measurements (i.e., the ratio of the measured transmissions) at $P = -20\,\text{dBm}$ and $P = +20\,\text{dBm}$, now for device A after all fabrication steps (step 6). This allows an easy identification of the resonance among a noisy background, since at larger incident power the superconductivity within the coplanar waveguide resonator breaks down first. The corresponding raw data for device A, step 6 at $P = -20\,\text{dBm}$ is plotted in Figure 2c.

Fano resonances in transmission, as observed in Figure 2, are a well-known phenomenon and are caused by parasitic channels bypassing the resonator. They can be modeled with the expression[14,15]

$$S_{21}(f) = \frac{A}{1 + 2iQ_c\,(f - f_0)/f_0} + re^{i\theta} \tag{1}$$

where A describes the overall transmission of the resonator, Q_c and f_0 are its quality factor and resonance frequency, and r and θ are the transmission amplitude and phase of the parasitic channel, respectively. For extracting the quality factors, we fit $|S_{21}(f)|^2$ to a selected interva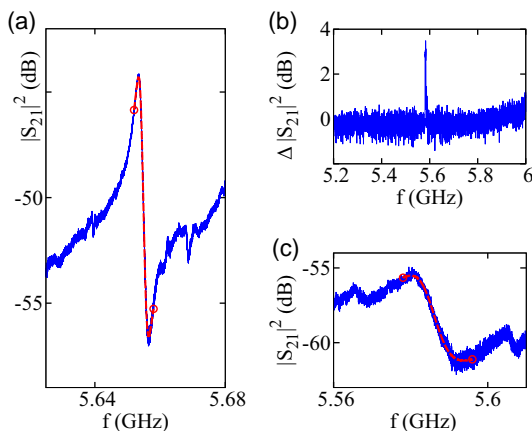l of the measurement data. Due to the varying and irregular signal background, this selection clearly influences the result; this is the main source of error for the extracted Q_c and the reason why only rounded values are given in Table 1. In Figure 2a,c, the red line indicates the best-fit function and the used interval.

The results are summarized in Table 1. Both devices start out at $Q_c \simeq 2500$. Device A retains $Q_c \simeq 1600$ until after the deposition of the central bias connection to the resonator. With the fabrication of the source/drain electrodes, however, the quality factor sharply drops to $Q_c \simeq 450$, a value quite close to the one observed in previous studies.[2,3] The quality factor of device B, initially similar as for device A, decreases with the deposition of the gate finger, but then remains near $Q_c \simeq 1600$ until the end of the fabrication.

We can conclude that the optimizations have a clear effect; after all lithographic steps, device B with its large, niobium-based filters and the shorter "coupling length" L of the electrodes, where they run parallel to the gate finger, has a quality factor higher by approximately a factor 3.5 compared to device A. In addition, since in device A the definition of the source/drain electrodes was the critical step reducing Q_c, it is likely that the reduction of L plays a role. From the experimental data, it is not possible yet to decide on the precise impact of the filter circuits.

5. Comparison with Numerical Modeling

To gain further insight into the nature of resonator losses and the effectiveness of the different types of filters, the software package Sonnet Professional[16] has been used to model a simplified circuit geometry. Sonnet uses the so-called method of moments[17,18] to calculate scattering matrix elements between circuit ports and is widely applied to problems in superconducting coplanar circuitry.

The substrate is modeled as stack of lossless insulators. The circuit geometry is segmented by the software in the initial calculation stages, with a minimum length scale set by user preference. To reduce calculation time we replace the fine gate finger electrode from the device geometries of Figure 1 as well as the contact electrodes with two 5 μm wide niobium stripes running in parallel at a distance of 2 μm for a length of L, see **Figure 3a**. In addition, for simplicity, the nanotube transfer region with contacts and filters is attached to a coplanar waveguide segment instead of a resonator.

Figure 3a shows the actual model geometry used in correspondence to device B. Ports 1 (signal input) and 2 (signal output) are $Z = 50\,\Omega$ terminated at the box walls of the calculated volume. A third port 3 connects the bond pad out of plane to ground; to approximate a dc wire connection, here, we assume a termination with $R_3 = 0$ as well as an inductance of $L_3 = 2\,\text{nH}$, the rule-of-thumb value for a 2 mm long wire bond.

In the variant of the geometry used for approximating device A, the niobium filter is replaced by a straight connection to the bond pad, and a fine gold meander identical to the one in the lithography drawing of device A is introduced directly at the edge of the transfer area.

Figure 3b,c displays the calculation result for the Au-based filter and the Nb-based filter geometry, respectively. Both geometries lead to a clear filter resonance in the region $6\,\text{GHz} \leq f_r \leq 7\,\text{GHz}$. The current density plotted in Figure 3a

Figure 2. Example VNA transmission measurements at $T = 4.2\,\text{K}$, with the device immersed into liquid helium. a) Device B, immediately after definition of the coplanar waveguide resonator (step 1); $P = -20\,\text{dBm}$, raw transmission data. b,c) Device A, after all fabrication (step 6). (b) Transmission difference of device A between measurements at VNA output power $-20\,\text{dBm}$ and $+20\,\text{dBm}$. (c) Raw data plot of device A for $P = -20\,\text{dBm}$. In (a) and (c), the red line indicates the fit function as well as the fitted region for the evaluation of Q_c.

ADVANCED
SCIENCE NEWS
www.advancedsciencenews.com
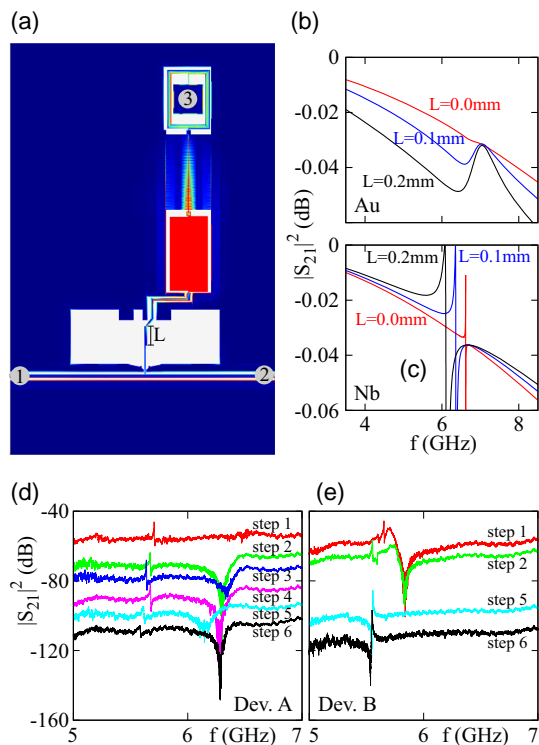
physica
pss
status
solidi
b
www.pss-b.com

Figure 3. Numerical modeling of strongly simplified circuits using Sonnet Professional.[16] a) Model geometry in the case of device B, including a segment of transmission line, a nanotube deposition area with closeby gate and contact electrodes ($L = 0.1$ mm), and a niobium T-filter with bond pad. Colors indicate the local current density at $f = 6.38$ GHz, the location of a filter resonance (red corresponds to high current density). b,c) Calculated power transmission $|S_{21}|^2$ from port 1 to port 2, for (b) the Au-based filter geometry (see text) and (c) the Nb-based filter geometry, in each case for $L = 0, 0.1, 0.2$ mm. d,e) Measured large frequency range transmission of (d) device A and (e) device B, following each fabrication step. The curves have been offset by 10 dB per step for visibility. Both the cavity resonance at $f \simeq 5.6$ GHz and the filter resonance are visible.

Figure 4. a) Model power transmission $|S_{21}|^2$ as function of frequency for the two filter types, at $L = 0.2$ mm. b) Model power transmission $|S_{21}|^2$ as function of coupling length L for the Nb-based filter, at $f = 5$ GHz and $f = 7$ GHz.

illustrates this at $f = 6.38$ GHz and $L = 0.1$ mm. For the resistive gold meander, Figure 3b, a strongly broadened Fano function results, with an initially decreasing transmission at low frequency as well as an overall decrease of transmission. Measurement of the transmission of device A over a large frequency range, see Figure 3d, indeed confirm the presence of such a filter resonance with the same behavior as soon as the gate finger electrode has been deposited and thus allows for a coupling between cavity and dc contact connections.

The filter resonance of the larger, niobium-based filter is considerably sharper due to the superconductivity of the material (modeled as lossless metal), see Figure 3c. In addition, the Fano behavior displays different polarity: the filter initially leads for frequencies below its resonance to suppressed damping, via constructive interference of the reflected signal. For larger L, the resonance moves to lower frequencies. Figure 3e, a measurement of device B, clearly agrees with this result for the first two fabrication steps.

The filter resonance appears to be absent after deposition of the source/drain contacts (step 5). While from the data no
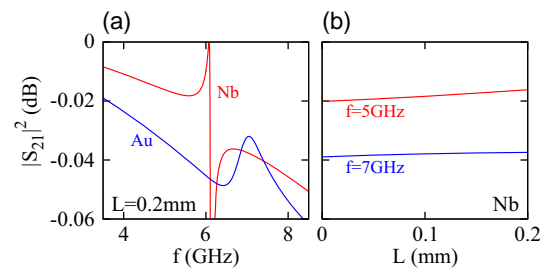
definite explanation for this can be given, a striking detail is that here also the Fano shape of the microwave cavity resonance has changed its polarity. Via the much stronger coupling of the cavity to the dc connection and its filter, the filter resonance may have moved to a significantly lower frequency. We can speculate that it may have merged with the cavity resonance or passed it entirely, with both signal contributions phase-shifted and again interfering constructively.

Additional modeling results are shown in **Figure 4**. The power transmission $|S_{21}|^2$ as function of frequency for the two filter types is compared in Figure 4a at $L = 0.2$ mm. Again, this plot clearly demonstrates that the Au-based filters lead to damping, while at proper choice of parameters the Nb-based filter reflects the GHz signal back into the circuit for constructive interference. Figure 4b plots the transmission for the Nb-based geometry as function of the coupling length L for $f = 5$ GHz and $f = 7$ GHz, i.e., below and above the filter resonances. As expected for the reflection mechanism, a stronger coupling of the dc connections here even counterintuitively improves the signal.

6. Conclusion and Outlook

Two coplanar waveguide resonator devices including dc electrodes for microwave optomechanical experiments involving carbon nanotubes have been fabricated, with tests of low-temperature GHz transmission properties after each step.[19] Device A, identical in geometry with the device of previous studies,[2,3] includes a resistive gold meander in the dc connections, device B a niobium-based T-filter. We show experimentally that the quality factor of device A sharply drops with the fabrication of the source/drain electrodes, while device B retains a significantly higher Q_c up to the end of processing.

Model calculations using Sonnet Professional[16] on a simplified device geometry confirm these results. While the gold-based filter geometry leads to damping of the reflected signal, the niobium-based geometry can better reflect the signal back into the circuit, for constructive interference, minimizing losses and thereby in a full device maximizing Q_c. For the latter effect, a filter resonance plays an important role, a fact that will have to be taken into account for future device geometry planning.

While for superconducting two-level systems already multiple mechanisms to enhance optomechanical coupling have been proposed and implemented,[20,21] for the particularly interesting

case of carbon nanotube resonators this research is still at the start. Aside from quantum capacitance effects,[2,3,22] also integrating carbon nanotubes as variable Josephson inductors is expected to lead to a strong coupling amplification.[23,24] In addition to a modified GHz circuit geometry, this requires transparent contacts between superconductor and carbon nanotube,[25–27] in a device that keeps the carbon nanotubes suspended and thus nanomechanically active. Recent results[28] with gate voltage-dependent critical currents in suspended, as-grown single-wall carbon nanotubes of up to 53 nA indicate that molybdenum-rhenium alloys[11,29] provide a solution to this challenge, showing the way toward future optomechanical hybrid devices.

Conflict of Interest

The authors declare no conflict of interest.

Data Availability Statement

The data that support the findings of this study are available from the corresponding author upon reasonable request.

[1] M. Aspelmeyer, T. J. Kippenberg, F. Marquardt, *Rev. Mod. Phys.* **2014**, *86*, 1391.

[2] S. Blien, P. Steger, N. Hüttner, R. Graaf, A. K. Hüttel, *Nat. Commun.* **2020**, *11*, 1363.

[3] N. Hüttner, S. Blien, P. Steger, R. Graaf, A. K. Hüttel, arXiv:2304.02748 [cond-mat] **2023**.

[4] A. K. Hüttel, G. A. Steele, B. Witkamp, M. Poot, L. P. Kouwenhoven, H. S. J. van der Zant, *Nano Lett.* **2009**, *9*, 2547.

[5] J. Moser, A. Eichler, J. Güttinger, M. I. Dykman, A. Bachtold, *Nat. Nanotechnol.* **2014**, *9*, 1007.

[6] E. A. Laird, F. Kuemmeth, G. A. Steele, K. Grove-Rasmussen, J. Nygård, K. Flensberg, L. P. Kouwenhoven, *Rev. Mod. Phys.* **2015**, *87*, 703.

[7] S. Blien, K. J. G. Götz, P. L. Stiller, T. Mayer, T. Huber, O. Vavra, A. K. Hüttel, *Phys. Status Solidi B* **2016**, *253*, 2385.

[8] S. Blien, P. Steger, A. Albang, N. Paradiso, A. K. Hüttel, *Phys. Status Solidi B* **2018**, *255*, 1800118.

[9] J. A. Brydson, *Plastics Materials*, 7th ed., Butterworth-Heinemann, Oxford, Boston **1999**.

[10] Y. Hao, F. Rouxinol, M. D. LaHaye, *Appl. Phys. Lett.* **2014**, *105*, 222603.

[11] K. J. G. Götz, S. Blien, P. L. Stiller, O. Vavra, T. Mayer, T. Huber, T. N. G. Meier, M. Kronseder, C. Strunk, A. K. Hüttel, *Nanotechnology* **2016**, *27*, 135202.

[12] D. C. Mattis, J. Bardeen, *Phys. Rev.* **1958**, *111*, 412.

[13] J. Gao, J. Zmuidzinas, A. Vayonakis, P. Day, B. Mazin, H. Leduc, *J. Low Temp. Phys.* **2008**, *151* 557.

[14] M. S. Khalil, M. J. A. Stoutimore, F. C. Wellstood, K. D. Osborn, *J. Appl. Phys.* **2012**, *111*, 054510.

[15] P. J. Petersan, S. M. Anlage, *J. Appl. Phys.* **1998**, *84*, 3392.

[16] Sonnet Software, Inc., Sonnet Professional 18.56, https://www.sonnetsoftware.com/ (accessed: April 2023).

[17] R. F. Harrington, *Field Computation by Moment Methods, IEEE Press Series on Electromagnetic Waves*, IEEE Press, Piscataway, NJ **1993**.

[18] J. Rautio, R. Harrington, *IEEE Trans. Microwave Theory Tech.* **1987**, *35*, 726.

[19] S. Reinhardt, C. Butschkow, S. Geissler, A. Dirnaichner, F. Olbrich, C. Lane, D. Schröer, A. K. Hüttel, *Comput. Phys. Commun.* **2019**, *234*, 216.

[20] J. M. Pirkkalainen, S. U. Cho, F. Massel, J. Tuorila, T. T. Heikkilä, P. J. Hakonen, M. A. Sillanpää, *Nat. Commun.* **2015**, *6*, 6981.

[21] P. Schmidt, M. T. Amawi, S. Pogorzalek, F. Deppe, A. Marx, R. Gross, H. Huebl, *Commun. Phys.* **2020**, *3*, 233.

[22] J. Manninen, M. T. Haque, D. Vitali, P. Hakonen, *Phys. Rev. B* **2022**, *105*, 144508.

[23] T. T. Heikkilä, F. Massel, J. Tuorila, R. Khan, M. A. Sillanpää, *Phys. Rev. Lett.* **2014**, *112*, 203603.

[24] A. J. Rimberg, M. P. Blencowe, A. D. Armour, P. D. Nation, *New J. Phys.* **2014**, *16*, 055008.

[25] M. R. Buitelaar, W. Belzig, T. Nussbaumer, B. Babić, C. Bruder, C. Schönenberger, *Phys. Rev. Lett.* **2003**, *91*, 057005.

[26] P. Jarillo-Herrero, J. A. van Dam, L. P. Kouwenhoven, *Nature* **2006**, *439*, 953.

[27] H. I. Jørgensen, K. Grove-Rasmussen, T. Novotný, K. Flensberg, P. E. Lindelof, *Phys. Rev. Lett.* **2006**, *96*, 207003.

[28] J. P. Kaikkonen, A. T. Sebastian, P. Laiho, N. Wei, M. Will, Y. Liao, E. I. Kauppinen, P. J. Hakonen, *Nano Res.* **2020**, *13*, 3433.

[29] B. H. Schneider, S. Etaki, H. S. J. van der Zant, G. A. Steele, *Sci. Rep.* **2012**, *2*, 599.